Partially Rated Power Flow Control Converter Modeling for Low Voltage DC Grids

Purgat, Pavel; van der Blij, Nils; Qin, Zian; Bauer, Pavol

DOI
10.1109/JESTPE.2019.2915166

Publication date
2019

Document Version
Final published version

Published in
IEEE Journal of Emerging and Selected Topics in Power Electronics

Citation (APA)
Purgat, P., van der Blij, N., Qin, Z., & Bauer, P. (2019). Partially Rated Power Flow Control Converter Modeling for Low Voltage DC Grids. *IEEE Journal of Emerging and Selected Topics in Power Electronics*, *8*(3), 2430-2444. Article 8708241. Advance online publication. https://doi.org/10.1109/JESTPE.2019.2915166

Partially Rated Power Flow Control Converter Modeling for Low-Voltage DC Grids

Pavel Purgat, *Student Member, IEEE*, Nils H. van der Blij, *Student Member, IEEE*, Zian Qin, *Member, IEEE*, and Pavol Bauer, *Senior Member, IEEE*

***Abstract*— Scalable and robust low-voltage direct current (LVdc) distribution networks require solutions, allowing flexible power flow control and reliable short-circuit protection. In this paper, the continuous full-order large- and small-signal models of a partially rated power flow control converter (PFCC) are derived utilizing the generalized averaging method. The large-signal model of the PFCC is coupled with a model of the LVdc grid. Due to the state-space representation, the combined model of the PFCC and the LVdc grid is suitable for easy algorithmization, and efficient simulation. These advantages make them essential tools for studying and optimizing of scalable LVdc systems with decentralized power flow control based on the PFCC. The PFCC models provide insights into controller design and stability analysis. The models are experimentally validated, and the functionality of the PFCC is demonstrated in a laboratory-scale microgrid.**

***Index Terms*— Direct current, low voltage, microgrid, modeling, power flow control.**

NOMENCLATURE

N	Nodes in the dc distribution grid.
l	Distribution lines in dc distribution grid.
o	Phase conductors in dc distribution grid.
m	Loads in dc distribution grid.
$\boldsymbol{\Gamma}$	Incidence matrix describing the connectivity of dc distribution grids.
$\boldsymbol{C}_N$	Diagonal capacitance matrix of dc distribution grid.
$\boldsymbol{G}_N$	Conductance matrix of dc distribution grid.
$\boldsymbol{V}_N$	Matrix of the node voltages in dc distribution grid.
$\boldsymbol{I}_N$	Matrix of the currents flowing into each node in dc distribution grid.
$\boldsymbol{I}_{\text{Line}}$	Matrix of the line currents in dc distribution grid.
$\boldsymbol{L}_l$	Diagonal inductance matrix of dc distribution grid.
$\boldsymbol{R}_l$	Diagonal resistance matrix of dc distribution grid.
$V_1, V_2, \ldots, V_i$	Node Voltages in the dc distribution grid.
$I_{\text{Line},1}, \ldots, I_{\text{Line},i}$	Line currents flowing on the positive rail in the dc distribution grid.
T_s	Switching period of the power flow control converter (PFCC).
f_s	Switching frequency.
f_c	Corner (cutoff) frequency.
t	Time.
Δt_i	Time interval.
τ	Time variable during switching period.
s	Complex number frequency parameter.
$\langle x \rangle_k$	The kth coefficient of the Fourier series.
ω_s	Angular frequency.
$s_1(\tau)$	Switching function of the high voltage side full bridge of the PFCC.
$s_2(\tau)$	Switching function of the low-voltage side full bridge of the PFCC.
$s_3(\tau)$	Switching function of the unfolder bridge of the PFCC.
φ	Phase shift of the dual active bridge (DAB) converter inside PFCC
d_1	Averaged control signal of the DAB inside PFCC.
d_2''	Duty cycle of the unfolding bridge inside PFCC.
d_2'	Averaged duty cycle of the unfolding bridge inside PFCC.
d_2	Averaged duty cycle of the unfolding bridge inside PFCC rewritten as $d_2 = 2d_2' - 1$.
v_{in}	Input voltage of the PFCC.
v_{dc}	Middle dc-link voltage of PFCC.
v_{series}	Output voltage of the PFCC.
i_{in}	Input current of PFCC.
i_σ	Leakage inductor current of the DAB inside PFCC.
$i_{\sigma,1R}$	Real part of the first coefficient of the Fourier series representing DAB leakage current.
$i_{\sigma,1I}$	Imaginary part of the first coefficient of the Fourier series representing DAB leakage current.

Manuscript received November 22, 2018; revised February 20, 2019 and April 14, 2019; accepted April 19, 2019. Date of publication May 7, 2019; date of current version August 4, 2020. This work was supported by the Framework of the Joint Programming Initiative ERA-Net Smart Grids Plus, with support from the European Unions Horizon 2020 Research and Innovation Programme. Recommended for publication by Associate Editor Carl N. M. Ho. *(Corresponding author: Pavel Purgat.)*

The authors are with the DC Systems, Energy Conversion and Storage Group, Delft University of Technology, 2628 Delft, The Netherlands (e-mail: p.purgat@tudelft.nl).

Color versions of one or more of the figures in this article are available online at http://ieeexplore.ieee.org.

Digital Object Identifier 10.1109/JESTPE.2019.2915166

i_f	Inductor current of the unfolding bridge inside PFCC.
n	Transformer ratio of the DAB inside PFCC.
C_{in}	Input capacitor of the DAB inside PFCC.
L_{in}	Input inductor of the DAB inside PFCC.
R_{in}	Parasitic input resistor of the DAB inside PFCC.
L_σ	Leakage inductor of the DAB inside PFCC.
R_σ	Parasitic leakage resistor of the DAB inside PFCC.
C_{dc}	Output capacitor of the DAB inside PFCC.
$L_{f,1}$, $L_{f,2}$	Filter inductors of the unfolding bridge inside PFCC.
L_f	Sum of filter inductors $L_{f,1}$ and $L_{f,2}$.
C_{series}	Output capacitor of the unfolding bridge inside PFCC.
R_f	Parasitic resistor of the unfolding bridge inside PFCC.
R_{pfc}	Parasitic resistor in the main current path of the PFCC.
L_{pfc}	Parasitic inductance in the main current path of the PFCC.
$\boldsymbol{A}$, $\boldsymbol{B}$, $\boldsymbol{C}$, $\boldsymbol{D}$, $\boldsymbol{N}$	Matrices of the state-space representation.
$\bar{x}$	Vector of state-space variables describing the PFCC in state-space representation.
$\bar{u}$	Vector of the PFCC inputs in the state-space representation.
$\bar{w}$	Vector of the disturbances in the state-space representation.
$\boldsymbol{E}$	Identity matrix.
$\boldsymbol{G}$	Matrix of transfer functions of small-signal model of PFCC.
$G_{1,1} - G_{2,4}$	Transfer functions of small-signal model of PFCC.
V^*_{dc}	Reference value for PFCC dc link voltage.
V^*_{series}	Reference value for PFCC series voltage.
ζ	Relative damping.
$K_{\text{dc},1}$	Proportional gain of the dc link voltage PI controller.
$K_{\text{dc},2}$	Integral gain of the dc link voltage PI controller.
$K_{\text{unf},1}$	Proportional gain of the series voltage PI controller.
$K_{\text{unf},2}$	Integral gain of the series voltage PI controller.
$Z_{\text{Line,i}}$	Impedance of distribution line i modeled with lumped element π model.
$R_{\text{Line,i}}$	Resistance of distribution line i.
L_{Line}	Inductance of distribution lines.
C_{Line}	Capacitance of distribution lines.
C_{Node}	Node capacitance on the dc grid side.
$P_{\text{Line},i}$	Power transferred in the line i.
$P_{\text{Node},i}$	Power supplied or sunk in the node i.
$V_{\text{DAB,HV}}$	Midpoint voltage of the high voltage bridge in the DAB.
$V_{\text{DAB,LV}}$	Midpoint voltage of the low-voltage bridge in the DAB.
V_{unf}	Midpoint voltage of the unfolder bridge.

I. Introduction

THE push for decarbonization of energy consumption fuels the introduction of renewable energy sources and furthers the electrification of virtually every part of the world economy. The push can be illustrated by the growing popularity of electric vehicles [1]. As a result, the distribution grid is exposed to an outburst of various power electronic-based interfaces [2]. On the distribution grid level, these lead to the reduction of the grids time constant, higher power peaks, and the introduction of a new type of participant—the prosumer. These developments pose a challenge to the traditional top-down approach to the design and operation of distribution systems [3], [4]. These developments incentivized the re-evaluation of the role of low-voltage direct current (LVdc) in the electric energy distribution [5], [6].

The role of LVdc for electric energy distribution is generally studied in the context of microgrids [7]. Microgrids are typically defined as entities that coordinate distributed energy generators, energy storage, and consumption in a consistent and decentralized way that reduces the control burden on the grid [8]. The contemporary research is for the most part oriented toward ensuring stable and efficient current sharing of the parallel connected converters [9], [10], and modeling and stability analysis of the LVdc systems [11], [12]. It should be noted that there are different conceptual approaches to organizing the dc distribution systems (or microgrids). Starting from the centralized solid-state transformer-enabled microgrids [13], multiterminal medium voltage dc [14], LVdc systems with a point-of-load-like structure [5], or highly modular decentralized LVdc multiterminal systems [7].

Modeling of LVdc microgrids has been studied mostly to obtain insights into the control design [4], or stability [11]. Most of the models used for the LVdc microgrids use different state-space approaches to modeling of LVdc grids and are limited to the monopolar systems [15], [16]. Recently, a generalized approach to modeling of the LVdc grids was introduced in [12], which allows for easy algorithmization in Python or MATLAB/Simulink as well as the incorporation of bipolar topologies.

Two basic approaches to modeling of the power electronic converters are switching models and average models. The switching models due to computational burden are too inefficient to be used as part of large systems such as microgrids. Average models can be obtained via an average switch, average inductor current or average state-space model. If the converter topology does not violate the small-signal ripple

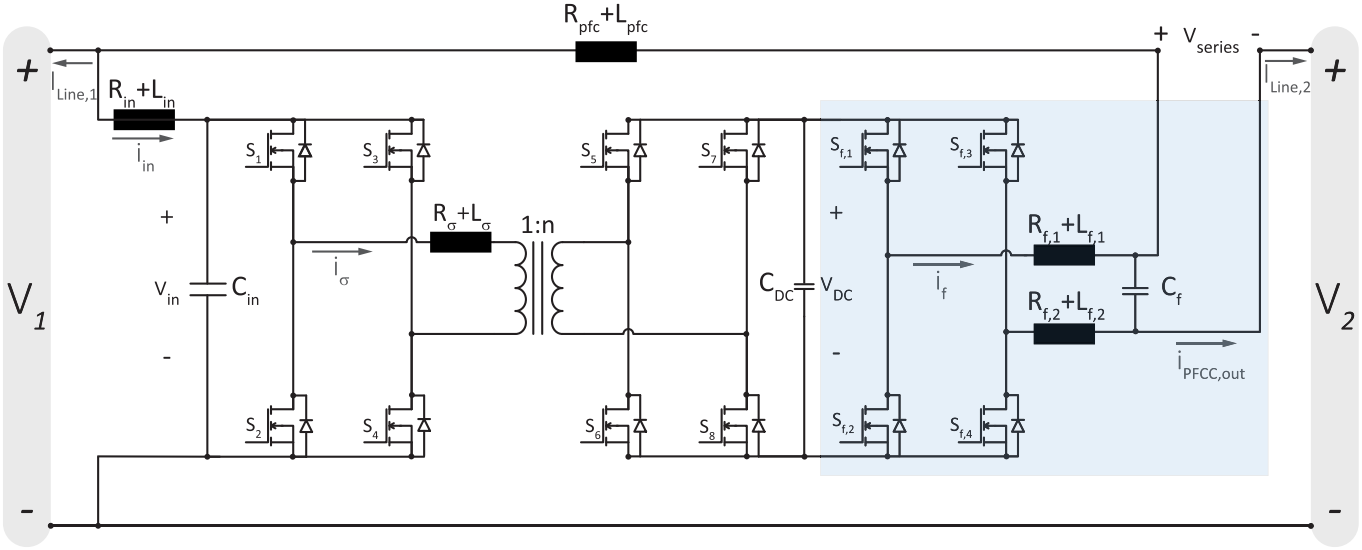

Fig. 1. PFCC for LVdc grids.

condition, then the use of various simplified average models presented in [17] are appropriate. However, when the topology such as dual active bridge (DAB) violates the condition, one needs to resort to reduced-order models neglecting the current dynamics such as [18] or full-order discrete-time models such as [19] or [20]. However, to gain the insights into control and stability of the converter, it is often desirable to have a continuous-time full-order model [21]. The generalized average modeling technique was applied to the DAB in [21]. Recently, it was improved to limit the small steady-state error in the closed-loop control signal of the DAB in [22] and even reformulated for the use with dc grid models in [23].

In any dc system, a challenge is to achieve efficient load sharing [10]. This challenge is enhanced when multiterminal (meshed) or ring topologies are used and is referred to as current limiting or power flow control [2], [24]. Power flows in meshed grids are coupled since the number of interconnection between nodes is higher than the number of nodes. Moreover, the nodes are not necessarily able to control the bus voltage, e.g., they behave like constant power loads or sources. Different approaches were already introduced for the power flow control, both for high-voltage dc and LVdc grids. The first method is based on changing the line resistance with a variable resistor and was described for both the HVdc [25], [26], and LVdc [24]. Naturally, such an approach is inherently inefficient. The second approach to be found in the available literature is to dedicate a dc–dc converter rated for the maximum power transferred through the network such as [27], [28]. There are several advantages when using a dedicated dc–dc converter rated for the full power of the system such as short-circuit protection integration. However, despite the advances in the power electronics, the cost and losses remain a bottleneck. Similar solutions using partially rated power flow control converters (PFCCs) were independently proposed for high-voltage dc and LVdc [24], [29]–[31]. The PFCC reduces losses from the system perspective with processing only a fraction of the power that it is controlling.

The partially rated PFCC is shown in Fig. 1. The partial power rating arises from its series-parallel connection with the grid. On one side, the converter is connected to the full grid voltage, but only a fraction of the nominal grid current is flowing inside the converter. On the other side of the step-down transformer, the converter is connected in series with a line. Thus, the current flowing on this side is the full network current. However, the operating voltage is a small fraction of the bus voltage. Achieving PFCC's partial power rating is straightforward with isolated topology. The transformer inside the PFCC provides the voltage step down and the galvanic isolation. The transformer is essential to create a floating voltage V_{series} and allows the use of voltage-derated components on the low-voltage side of the PFCC. The isolation of the transformer needs to withstand the full grid voltage. A similar concept can be used in HVdc systems; however, the transformer manufacturing complexity and cost would increase. The DAB topology is preferred due to its symmetry which offers easy implementation of bidirectional power flow, and further advantages are a low number of passive components and high power efficiency resulting from zero-voltage switching. The DAB is connected to the line via the unfolder full bridge. The unfolder bridge expands the operation of the PFCC into all four regions and extends the soft-switching operating area of the DAB by ensuring that the DAB operates with the unity of the voltage ratio. The operating range of V_{series} is dependent on the operating range of the bus voltage in the LVdc grid. Furthermore, the power that is processed by the PFCC is dependent on the maximum line current and the line impedance of the LVdc grid. The concrete minimum and maximum power rating of the PFCC, therefore, arises from the parameters of the grid in which it is installed.

A similar concept was proposed for ac networks in 1995 [32]. The unified power flow controller (UPFC) was presented as a generalization of the static synchronous compensator devices. The UPFC is connected to the network via 50-Hz transformers on both sides. The UPFC uses a common dc-link between the series and parallel connection to control the reactive and active power in the ac network. The heart of the UPFC and the PFCC is the concept of differential power processing [33]. This concept, however, is more interesting for LVdc, as there is no need for bulky 50-Hz transformers, and the protection scheme can be simplified [34]. The effect of series-parallel PFCCs on the HVdc grid was studied in [35] and [36]. Both [35] and [36] focus on the grid-level effects and formulation of the power flow control problem. The series-parallel converter is modeled as a general dc–dc converter, represented by controlled voltage and current sources. It was not the goal in this earlier work to consider and model the peculiarities of different topologies that are applicable for power flow control in HVdc or LVdc.

The main contributions of this paper are the derivation and experimental verification of the average full-order large-signal and small-signal models of the PFCC. Furthermore, the large-signal model of the PFCC is coupled with the LVdc grid model from [12]. As a result of state-space representation, the combined model allows easy simulation algorithmization, controller design, and stability analysis of the PFCC controlled LVdc grids in Python or MATLAB/Simulink, even for very complex systems. The PFCC models are validated by measuring the magnitude of the small-signal transfer functions. Furthermore, the models are validated via comparison of the dynamic performance in the laboratory-scale microgrid. In addition, the functionality of the PFCC in the meshed microgrid is demonstrated in experiments and simulations.

The rest of this paper is organized as follows. Section II recapitulates and explains the state-space model of LVdc grid and presents the derivation of the PFCC models with validation with the measured transfer functions. In Section III, the coupled model of the PFCC in the LVdc grid is used to simulate a simple meshed microgrid. These results are verified with experiments in Section IV. Last, Section V summarizes the paper and provides an outlook on the application of the models and the PFCC in the future.

II. Modeling

A. Modeling DC Distribution Grid

An example of a dc distribution system consisting of three nodes is shown in Fig. 2. Any dc distribution system can be described by its N nodes, l distribution lines, o phase conductors, and m loads and sources (which are connected to the nodes via power electronic converters). For simplicity's sake, the model is derived using a system that has a single-phase conductor (i.e., a monopolar system). However, the models presented in this section can readily be extended to multiple phase conductors [37].

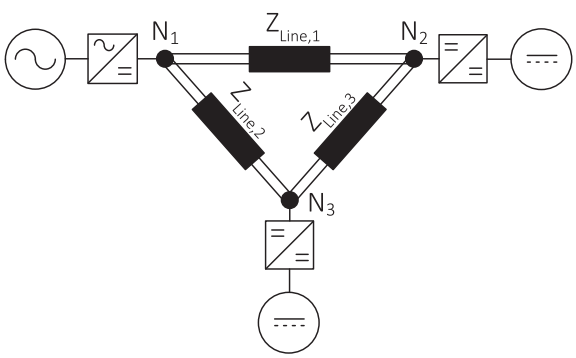

Fig. 2. Example of a bipolar dc distribution system containing three nodes and three lines.

To describe the connectivity of dc distribution systems, a so-called incidence matrix $\mathbf{\Gamma}$ is used

$$\mathbf{\Gamma}(j,i) = \begin{cases} 1 & \text{if } \mathrm{I}_{\mathrm{Line},j} \text{ is flowing from node } i \\ -1 & \text{if } \mathrm{I}_{\mathrm{Line},j} \text{ is flowing into node } i \\ 0 & \text{otherwise} \end{cases} \quad (1)$$

where i and j are the indices for each node and distribution line, respectively. Therefore, $I_{\mathrm{Line},j}$ indicates the current flowing in the distribution line j. Furthermore, the boldface of variables indicates that they are vectors or matrices.

A lumped element π model is used for modeling the system's distribution lines. This lumped element model is valid when the length of the line is much shorter than the wavelength of the signals [37], [38]. Consequently, the dynamic behavior of dc distribution systems can be described by the differential equations of their node voltages and line currents.

The differential equations that describe the node voltages in the system are given by

$$\boldsymbol{C}_N \frac{d}{dt}\boldsymbol{V}_N = \boldsymbol{I}_N - \mathbf{\Gamma}^{\boldsymbol{T}} \boldsymbol{I}_{\mathrm{Line}} - \boldsymbol{G}_N \boldsymbol{V}_N \quad (2)$$

where $\boldsymbol{C}_N$ is the (diagonal) capacitance matrix, $\boldsymbol{G}_N$ is the conductance matrix, $\boldsymbol{V}_N$ are the node voltages, $\boldsymbol{I}_N$ are the currents flowing into each node (from the connected converters), and $\boldsymbol{I}_{\mathrm{Line}}$ are the line currents.

The currents of the distribution lines are described by the differential equations

$$\boldsymbol{L}_l \frac{d}{dt}\boldsymbol{I}_{\mathrm{Line}} = \mathbf{\Gamma}\boldsymbol{V}_N - \boldsymbol{R}_l \boldsymbol{I}_{\mathrm{Line}} \quad (3)$$

where $\boldsymbol{L}_l$ and $\boldsymbol{R}_l$ are the (diagonal) inductance and resistance matrices, respectively.

Subsequently, a state-space model of the whole dc distribution system can be derived. The voltages at the nodes and the currents in the lines are chosen as the state variables. The complete state space formulation is then given by

$$\frac{d}{dt}\begin{bmatrix} \boldsymbol{V}_N \\ \boldsymbol{I}_{\mathrm{Line}} \end{bmatrix} = \begin{bmatrix} -\boldsymbol{C}_N^{-1}\boldsymbol{G}_N & -\boldsymbol{C}_N^{-1}\mathbf{\Gamma}^{\boldsymbol{T}} \\ \boldsymbol{L}_l^{-1}\mathbf{\Gamma} & -\boldsymbol{L}_l^{-1}\boldsymbol{R}_l \end{bmatrix}\begin{bmatrix} \boldsymbol{V}_N \\ \boldsymbol{I}_{\mathrm{Line}} \end{bmatrix} + \begin{bmatrix} \boldsymbol{C}_N^{-1} \\ \boldsymbol{\emptyset} \end{bmatrix}\boldsymbol{I}_N. \quad (4)$$

State-space models, like the one presented in 4, can be efficiently applied for stability studies by inspecting the eigenvalues. Moreover, stability can be analyzed analytically or by

using a root-locus method. This state-space dc distribution system model outputs the line currents and node voltages as a function of the currents flowing into each node ($\boldsymbol{I_N}$). Consequently, this system model can interface with any converter model that outputs a current as a function of the node voltage.

B. Power Flow Control Converter Model

The PFCC shown in Fig. 1 consists of two stages. The first stage is a DAB converter and the second is a full bridge converter that expands the operation of the PFCC into all four quadrants. Furthermore, the unfolder bridge extends the soft-switching operation region of the DAB, by ensuring that the DAB operates close to the unity voltage ratio. The DAB is connected to the total grid voltage on one side, but only, e.g., 10% of the rated current flows in. Inside the DAB, the step-down transformer provides the galvanic isolation and the necessary voltage ratio between the series and parallel connection of the PFCC. The DAB low-voltage bridge is connected through a decoupling capacitor to the unfolder bridge. The unfolder bridge and the DAB low-voltage side have to sustain the rated grid current; however, only a fraction of the grid voltage. Therefore, it is possible to use voltage-derated components on the LV side of the PFCC.

1) Recapitulation of Generalized Average Modeling: The generalized average modeling method was derived in [39], motivated by the switching circuits that did not fulfill the small-ripple condition. The generalized average modeling method was applied to the DAB in [21]. These models were used to connect full bridge inverter and DAB back-to-back in [40]. A considerable advantage of the generalized averaging method is that the standard state-space averaging is just a special case [39]. Thus, one method can be applied for all variables in PFCC.

Because, in the case of the DAB, the ac ripple in the current is far from being negligible, the generalized average modeling method needs to be applied. The core idea is to represent the state-space variable during the switching interval $t - T_s \leq \tau < t$ using Fourier series approximation

$$x(\tau) = \sum_{k=-\infty}^{\infty} \langle x \rangle_k(t) e^{-jk\omega_s \tau} \tag{5}$$

where $\langle x \rangle_k$ is the kth coefficient of the Fourier series and can be expressed as

$$\begin{aligned} \langle x \rangle_k(t) &= \frac{1}{T_s} \int_{t-T_s}^{t} x(\tau) e^{-jk\omega_s \tau} d\tau \\ &= \frac{1}{T_s} \int_{t-T_s}^{t} x(\tau) \cos(k\omega_s \tau) d\tau \\ &\quad - \frac{j}{T_s} \int_{t-T_s}^{t} x(\tau) \sin(k\omega_s \tau) d\tau. \end{aligned} \tag{6}$$

As shown, for example, in [39] or [21] using $\langle (d)/(dt)x \rangle_k(t)$ as representative of the average of the differential state variable, the derivative of the state-space variable is derived as

$$\frac{d}{dt}\langle x \rangle_k(t) = \left\langle \frac{d}{dt} x \right\rangle_k (t) - j\omega_s \langle x \rangle_k(t). \tag{7}$$

The kth coefficient of the product of the two variables x and y is

$$\langle xy \rangle_k = \sum_{i=-\infty}^{\infty} \langle x \rangle_{k-i} \langle y \rangle_i. \tag{8}$$

If the first positive and the first negative coefficients in Fourier series are complex conjugates, then the product of the zeroth coefficients becomes

$$\langle xy \rangle_0 = \langle x \rangle_0 \langle y \rangle_0 + 2(\langle x \rangle_{1R} \langle y \rangle_{1R} + \langle x \rangle_{1I} \langle y \rangle_{1I}). \tag{9}$$

For the first coefficients, the products become

$$\langle xy \rangle_{1R} = \langle x \rangle_0 \langle y \rangle_{1R} + \langle x \rangle_{1R} \langle y \rangle_{1I} \tag{10}$$

$$\langle xy \rangle_{1I} = \langle x \rangle_0 \langle y \rangle_{1I} + \langle x \rangle_{1I} \langle y \rangle_{1I}. \tag{11}$$

The subscripts "R" and "I" represent the real and the imaginary parts of the complex numbers, respectively. These are necessary preliminaries to deploy the PFCC model in the Large-Signal Model subsection.

2) Large-Signal Model: The generalized average modeling approach that was summarized in the previous section will be applied to the circuit from Fig. 1. The model of the PFCC in this paper is derived under the assumption that the magnetizing current in the transformer is negligible. For all MOSFETs in the PFCC, it is assumed that the voltage drop across the MOSFETs' diodes is insignificant and that the MOSFETs' switching transients are insignificant. The voltages in the PFCC are referred to the low-voltage side and where appropriate are divided by n-turns ratio of the transformer. The parasitic resistances of the MOSFETs and the transformer of the DAB are all lumped into one parasitic element referred to as R_σ, while the parasitic resistances of the MOSFETs and the filter inductors of the unfolder bridge are lumped into R_f.

When using the phase shift modulation for control of the DAB, the voltage on the high voltage $v_{hv}(\tau) = s_1(\tau) v_{c_1}(\tau)$ is achieved through the switching action, which is defined as

$$s_1(\tau) = \begin{cases} 1 & \text{in } 0 \leq \tau < \dfrac{T_s}{2} \\ -1 & \text{in } \dfrac{T_s}{2} < \tau < T_s. \end{cases} \tag{12}$$

On the low-voltage side, the voltage $v_{lv}(\tau) = s_2(\tau) v_{\mathrm{dc}}(\tau)$ is achieved through the switching action, which is defined as

$$s_2(\tau) = \begin{cases} 1 & \text{in } \dfrac{\varphi T_s}{2} \leq \tau < \dfrac{T_s}{2} + \dfrac{\varphi T_s}{2} \\ -1 & \text{in } 0 \leq \tau < \dfrac{\varphi T_s}{2} \quad \text{and} \quad \dfrac{T_s}{2} + \dfrac{\varphi T_s}{2} \leq \tau < T_s. \end{cases} \tag{13}$$

The voltage between the midpoints of the unfolder bridge is defined as a product of the switching coefficient $s_3(\tau)$ and the voltage v_{dc}. The switching coefficient is defined as

$$s_3(\tau) = \begin{cases} 1 & \text{in } 0 \leq \tau < d_2'' T_s \\ -1 & \text{in } d_2'' T_s < \tau < T_s. \end{cases} \tag{14}$$

The operation of the PFCC can be described with the following equations:

$$L_{\mathrm{in}} \frac{d}{d\tau} i_{\mathrm{in}}(\tau) = v_1(\tau) - v_{\mathrm{in}}(\tau) - R_{\mathrm{in}} i_{\mathrm{in}}(\tau) \tag{15}$$

$$C_{\text{in}}\frac{d}{d\tau}v_{\text{in}}(\tau) = i_{\text{in}}(\tau) - s_1(\tau)i_\sigma(\tau) \tag{16}$$

$$L_\sigma\frac{d}{d\tau}i_\sigma(\tau) = -R_\sigma i_\sigma(\tau) + v_{hv}(\tau) - nv_{lv}(\tau) \tag{17}$$

$$C_{\text{dc}}\frac{d}{d\tau}v_{\text{dc}}(\tau) = s_2(\tau)ni_\sigma(\tau) + s_3(\tau)i_f \tag{18}$$

$$L_{\text{f}}\frac{d}{d\tau}i_f(\tau) = -R_f i_f(\tau) + v_{\text{dc}}(\tau)s_3(\tau) - v_{\text{series}}(\tau) \tag{19}$$

$$C_{\text{f}}\frac{d}{d\tau}v_{\text{series}}(\tau) = \frac{1}{R_{\text{pfc}}}\left[v_2(\tau) - v_1(\tau) + v_{\text{series}}(\tau)\right] + i_f(\tau). \tag{20}$$

In (15)–(20), the role of L_{pfc} is neglected. The reason is that the connection is short, and is separated by the capacitors on each side. Therefore, to keep the number of state-space variables low, it is not used explicitly. The derivation of the average large-signal model of the PFCC is completed with the introduction of the Fourier coefficients of the switching signals $s_1(\tau)$, $s_2(\tau)$, and $s_3(\tau)$. For the coefficients of $s_1(\tau)$ and $s_2(\tau)$, it is assumed, as in [21], that the duty ratio is fixed at 50%. Consequently, the coefficients are

$$\langle s_1\rangle_0 = \langle s_1\rangle_{1R} = \langle s_2\rangle_0 = 0 \tag{21}$$

and

$$\langle s_1\rangle_{1I} = -\frac{2}{\pi} \tag{22}$$

$$\langle s_2\rangle_{1R} = -\frac{2\sin(d_1\pi)}{\pi} \tag{23}$$

$$\langle s_2\rangle_{1I} = -\frac{2\cos(d_1\pi)}{\pi}. \tag{24}$$

For the unfolder bridge, the Fourier coefficients are

$$\langle s_3\rangle_0 = 2d_2' - 1 \tag{25}$$

$$\langle s_3\rangle_{1R} = \frac{\sin(2\pi d_2')}{\pi} \tag{26}$$

$$\langle s_3\rangle_{1I} = -\frac{2}{\pi}\sin^2\left(\pi d_2'\right). \tag{27}$$

Applying the generalized average modeling method on the PFCC is somewhat cumbersome. Therefore, the equations are not presented herein detail to keep the description concise. The average model of the PFCC is simplified by assuming that besides the DAB transformer current i_σ, it is appropriate to represent the variables by their zero-order terms, as was done, for example, in [21]. The main difference between the DAB transformer current and other currents in the model is that, in the DAB, it is only ac components that transfer power, while its dc component is equal to zero. The precision of the modeling can be improved by including the ac components of other variables. However, that would make the model unnecessarily complicated and as is argued in [21] with limited gains in precision.

In the following equations, the control signal of the unfolder bridge is rewritten as $d_2 = 2d_2' - 1$. The PFCC is described in the matrix form

$$\frac{d}{dt}\bar{x} = \boldsymbol{A}\bar{x} + \boldsymbol{B}\bar{u}$$

where

$$\bar{x} = \begin{bmatrix} i_{\text{in}} & v_{\text{in}} & v_{\text{dc}} & i_{\sigma,1R} & i_{\sigma,1I} & i_f & v_{\text{series}}\end{bmatrix}$$
$$\bar{u} = \begin{bmatrix} v_1 & v_2\end{bmatrix}.$$

In vectors $\bar{x}$ and $\bar{u}$, only the DAB inductor current is modeled with ac components $i_{\sigma,1R}$, $i_{\sigma,1I}$. The rest of the variables is represented by the zeroth order coefficient which is dominant. The matrices $\boldsymbol{A}$ and $\boldsymbol{B}$ are in (28) shown at the bottom of this page.

$$\boldsymbol{A} = \begin{bmatrix} -\frac{R_{\text{in}}}{L_{\text{in}}} & -\frac{1}{L_{\text{in}}} & 0 & 0 & 0 & 0 & 0 \\ \frac{1}{C_{\text{in}}} & 0 & 0 & 0 & \frac{4}{\pi C_{\text{in}}} & 0 & 0 \\ 0 & 0 & 0 & -\frac{4n}{\pi C_{\text{dc}}}\sin(d_1\pi) & -\frac{4n}{\pi C_{\text{dc}}}\cos(d_1\pi) & \frac{d_2}{C_{dc}} & 0 \\ 0 & 0 & \frac{2n}{\pi L_\sigma}\sin(d_1\pi) & \frac{-R_\sigma}{L_\sigma} & \omega_s & 0 & 0 \\ 0 & -\frac{2}{\pi L_\sigma} & -\frac{2n}{\pi L_\sigma}\cos(d_1\pi) & -\omega_s & \frac{-R_\sigma}{L_\sigma} & 0 & 0 \\ 0 & 0 & \frac{d_2}{L_f} & 0 & 0 & -\frac{R_f}{L_f} & \frac{1}{L_f} \\ 0 & 0 & 0 & 0 & 0 & \frac{1}{C_f} & -\frac{1}{R_{\text{pfc}}C_f} \end{bmatrix}$$

$$\boldsymbol{B} = \begin{bmatrix} \frac{1}{L_{\text{in}}} & 0 \\ 0 & 0 \\ 0 & 0 \\ 0 & 0 \\ 0 & 0 \\ 0 & 0 \\ -\frac{1}{R_{\text{pfc}}C_{\text{f}}} & \frac{1}{R_{\text{pfc}}C_{\text{f}}} \end{bmatrix} \tag{28}$$

3) Small-Signal Model: To derive the small-signal average model of the converter, we first define the small-signal deviations as

$$\begin{aligned}
\Delta d_1 &= d_1 - D_1 \\
\Delta d_2 &= d_2 - D_2 \\
\Delta v_{in} &= v_{\text{in}} - V_{\text{in}} \\
\Delta i_{in} &= i_{\text{in}} - I_{\text{in}} \\
\Delta v_{\text{dc}} &= v_{\text{dc}} - V_{\text{dc}} \\
\Delta i_{\sigma,1R} &= i_{\sigma,1R} - I_{\sigma,1R} \\
\Delta i_{\sigma,1I} &= i_{\sigma,1I} - I_{\sigma,1I} \\
\Delta i_f &= i_f - I_f \\
\Delta v_{\text{series}} &= v_{\text{series}} - V_{\text{series}} \\
\Delta v_1 &= v_1 - V_1 \\
\Delta v_2 &= v_2 - V_2
\end{aligned}$$

where Δ defines the small-signal state, the uppercase letters represent the dc terms, and the lowercase letters the large-signal states.

Since the PFCC's mathematical description contains multiplication of the two state variables, it is necessary to define the following:

$$\begin{aligned}
\sin(\pi d_1)v_{\text{dc}} = \sin(\pi D_1)\Delta v_{\text{dc}} + V_{\text{dc}}\sin(\pi D_1) \\
+ V_{\text{dc}}\cos(\pi D_1)(\pi \Delta d_1).
\end{aligned} \quad (29)$$

The small-signal model of the PFCC is given in the matrix form

$$\frac{d}{dt}\Delta\bar{x} = \boldsymbol{A}\Delta\bar{x} + \boldsymbol{B}\Delta\bar{u} + \boldsymbol{N}\Delta\bar{w} \quad (30)$$

where

$$\begin{aligned}
\Delta\bar{x} &= \begin{bmatrix}\Delta i_{\text{in}} & \Delta v_{\text{in}} & \Delta v_{\text{dc}} & \Delta i_{\sigma,1R} & \Delta i_{\sigma,1I} & \Delta i_f & \Delta v_{\text{series}}\end{bmatrix} \\
\Delta\bar{u} &= \begin{bmatrix}\Delta d_1 & \Delta d_2\end{bmatrix} \\
\Delta\bar{w} &= \begin{bmatrix}\Delta v_1 & \Delta v_2\end{bmatrix}
\end{aligned}$$

and the matrices $\boldsymbol{A}$, $\boldsymbol{B}$, and $\boldsymbol{N}$ are in (31) shown at the bottom of this page.

The transfer functions between control inputs and output voltages, when the disturbances on voltages V_1 and V_2 are neglected, are obtained using the well-known relation for the transfer function matrices

$$\boldsymbol{G}(s) = \boldsymbol{C}\,(\boldsymbol{E}s - \boldsymbol{A})^{-1}\,\boldsymbol{B} \quad (32)$$

where s is the complex variable in Laplace domain.

In order to measure the ratio between controlled voltages and the control signals, the matrix $\boldsymbol{C}$ is defined as

$$\boldsymbol{C} = \begin{bmatrix}0 & 0 & 1 & 0 & 0 & 0 & 0\\ 0 & 0 & 0 & 0 & 0 & 0 & 1\end{bmatrix}$$

then, the transfer function matrix becomes

$$\boldsymbol{G}(s) = \begin{bmatrix}G_{1,1}(s) & G_{1,2}(s)\\ G_{2,1}(s) & G_{2,2}(s)\end{bmatrix} = \begin{bmatrix}\dfrac{\Delta v_{\text{dc}}}{\Delta d_1} & \dfrac{\Delta v_{\text{dc}}}{\Delta d_2}\\ \dfrac{\Delta v_{\text{series}}}{\Delta d_1} & \dfrac{\Delta v_{\text{series}}}{\Delta d_2}\end{bmatrix}. \quad (33)$$

$$\boldsymbol{A} = \begin{bmatrix}
-\dfrac{R_{\text{in}}}{L_{\text{in}}} & -\dfrac{1}{L_{\text{in}}} & 0 & 0 & 0 & 0 & 0 \\
\dfrac{1}{C_{\text{in}}} & 0 & 0 & 0 & \dfrac{4}{\pi C_{\text{in}}} & 0 & 0 \\
0 & 0 & 0 & -\dfrac{4n}{\pi C_{\text{dc}}}\sin(D_1\pi) & -\dfrac{4n}{\pi C_{\text{dc}}}\cos(D_1\pi) & \dfrac{D_2}{C_{dc}} & 0 \\
0 & 0 & \dfrac{2n}{\pi L_\sigma}\sin(D_1\pi) & \dfrac{-R_\sigma}{L_\sigma} & \omega_s & 0 & 0 \\
0 & -\dfrac{2}{\pi L_\sigma} & -\dfrac{2n}{\pi L_\sigma}\cos(D_1\pi) & -\omega_s & \dfrac{-R_\sigma}{L_\sigma} & 0 & 0 \\
0 & 0 & \dfrac{D_2}{L_f} & 0 & 0 & -\dfrac{R_f}{L_f} & \dfrac{1}{L_f} \\
0 & 0 & 0 & 0 & 0 & \dfrac{1}{C_f} & -\dfrac{1}{R_{\text{pfc}}C_f}
\end{bmatrix}$$

$$\boldsymbol{B} = \begin{bmatrix}
0 & 0 \\
0 & 0 \\
-\dfrac{4n}{\pi C_{\text{dc}}}\left(I_{\sigma,1I}\sin(\pi D_1) - I_{\sigma,1R}\cos(\pi D_1)\right) & \dfrac{I_{\text{f}}}{C_{\text{dc}}} \\
\dfrac{2\,n}{L_\sigma}V_{\text{dc}}\cos(\pi D_1) & 0 \\
-\dfrac{2\,n}{L_\sigma}V_{\text{dc}}\sin(\pi D_1) & 0 \\
0 & \dfrac{V_{\text{dc}}}{L_f} \\
0 & 0
\end{bmatrix}, \boldsymbol{N} = \begin{bmatrix}
\dfrac{1}{L_{\text{in}}} & 0 \\
0 & 0 \\
0 & 0 \\
0 & 0 \\
0 & 0 \\
0 & 0 \\
-\dfrac{1}{R_{\text{pfc}}C_{\text{f}}} & \dfrac{1}{R_{\text{pfc}}C_{\text{f}}}
\end{bmatrix} \quad (31)$$

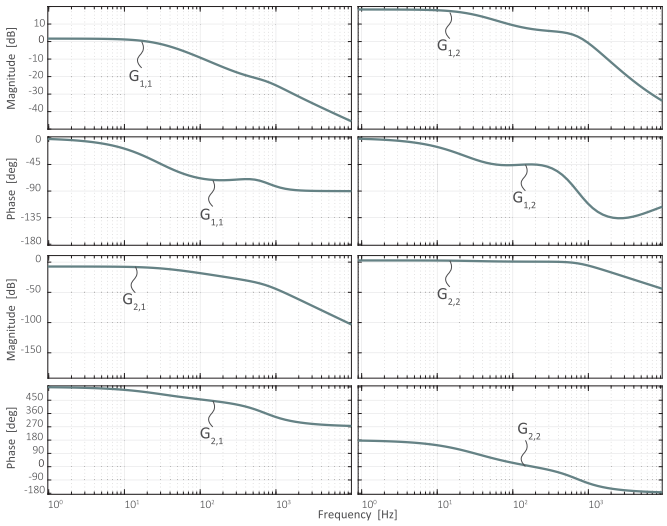

Fig. 3. Calculated control-to-output gains and phases of the partially rated PFCC.

Fig. 3 shows the complete set of calculated control-to-output gains of the PFCC. Due to stability of the measured plant, it is impractical to measure transfer functions of the PFCC in open-loop, the transfer function of the DAB and unfolder are measured separately. The transfer functions were measured using the Bode 100 vector analyzer. The measurement of the transfer functions with Bode 100 is described, for example, in [41]. The comparison of the measured and simulated transfer functions is shown in Fig. 4. It is clear from the figures that the measurement and simulation show an excellent match. The somewhat low crossover frequency is caused by the considerable size of the capacitor bank of the prototype PFCC.

III. Simulation

In Section II, models of dc grid and large-signal model of PFCC were developed. In this section, the dc grid model is used together with the PFCC large-signal model to demonstrate the usefulness of the derived models and validate the models in the time domain. The section starts with a brief discussion on how the PFCC small-signal model can be used to choose the closed-loop controllers and their parameters. Closing the control loops of the PFCC is necessary to compare the measured and simulated step-response of the PFCC. Furthermore, the closed-loop control allows simulating simple multiterminal LVdc grids with the PFCC to show the functionality of the PFCC. In the last section, the sensitivity of the models to the line parameters is discussed as the line parameters can influence the operation and the measurement results.

A. PFCC Control

The averaged small-signal models derived in Section II are used here to choose closed-loop controllers for the PFCC. The PFCC has a middle-link dc voltage, which is the output of the DAB. The DAB implements a simple phase shift modulation. Fig. 4(a) shows the DAB converter control-to-output transfer function. Increasing the switching frequency f_s of the DAB results in decreasing the leakage inductance L_σ needed to transfer the amount of power. Thus, changes in the switching frequency and leakage inductance cancel each other out. As is visible from the transfer function $G_{1,1}(s)$ in Fig. 4(a), DAB has one significant pole, which is dominated by the output capacitance. Increasing the size of the output capacitor C_{dc} limits the bandwidth of DAB even further. The fact that DAB has only one significant pole means that a PI controller is a good starting candidate for the control of voltage V_{dc}. The developed models allow to investigate the influence of other parameters on the voltage V_{dc} such as Δd_2, Δv_1 and Δv_2. A short design procedure based on [42] follows. The equation of PI controller for V_{dc} is

$$C_{\mathrm{PI,dc}}(s) = K_{\mathrm{dc},1} + \frac{K_{\mathrm{dc},2}}{s}. \tag{34}$$

Fig. 4(a) exhibits one significant pole, and the corner frequency can be found in the point for which the magnitude falls by -3 dB. The design procedure in [42] can be simplified, and the proportional gain $K_{\mathrm{dc},1}$ can be written

$$K_{\mathrm{dc},1} = \frac{f_c \zeta}{2\pi f_o} \tag{35}$$

where ζ is the relative damping and typically is chosen to be $(1)/(\sqrt{2})$, f_o stands for natural system frequency, and f_c stands for the corner frequency. The integral gain is then

$$K_{\mathrm{dc},2} = \frac{1}{\pi f_o}\left(\frac{\pi}{2} f_c\right)^2. \tag{36}$$

The unfolder bridge operates with bipolar modulation. Inspecting Fig. 4(b), unfolder bridge exhibits one significant pole which is dominated by the output capacitance. The influence of the filter inductor is attenuated by parasitic resistance. To control voltage V_{series} it sufficient to use a PI controller. The procedure outlined in equations 35 and 36 or algebra-on-the-graph method can be used to choose $K_{\mathrm{unf},1}$ and $K_{\mathrm{unf},2}$. The PI controllers can be prone to high-frequency disturbances. In this paper, we assume that the LVdc grid is strongly capacitive, and there are no high-frequency disturbances. The control loops used in this paper are kept simple since the PFCC control is not the primary focus of the paper. This section briefly demonstrated that the derived PFCC small-signal model is suitable to design the PFCC controllers.

As was explained in Section II of this paper, the converter models in the grid need to use node voltages as their inputs and node currents as their output to the dc grid model. From Figs. 1 and 5, it should be clear that the voltages V_1, V_2, highlighted in blue, are the inputs from the dc grid model to the PFCC model. The currents flowing out of the PFCC, highlighted in green, are the outputs of the large-signal PFCC model to the grid model. These currents can be specified from the derived large-signal PFCC model. For the current $I_{\mathrm{Line},2}$, we can write

$$I_{\mathrm{Line},2} = \frac{1}{R_{\mathrm{pfc}}}\left(V_2 - V_1 + v_{\mathrm{series}}\right) \tag{37}$$

And, for the current in the line 1, we can write

$$I_{\mathrm{Line},1} = I_{\mathrm{Line},2} - i_{\mathrm{in}}. \tag{38}$$

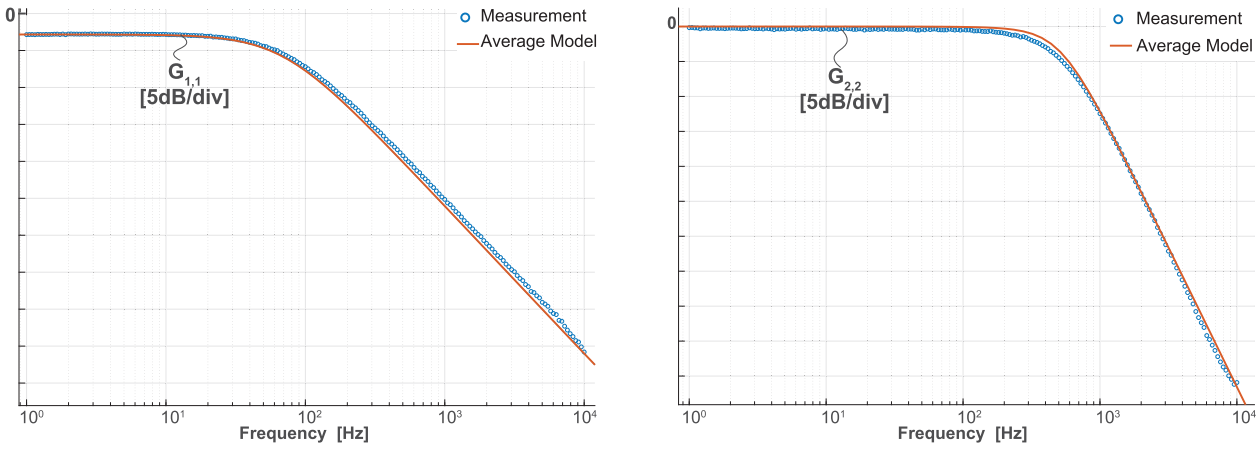

Fig. 4. Comparison of the magnitude of the measured and simulated transfer functions of the PFCC. (a) Measured and the calculated transfer function between the control signal d_1 and the voltage v_{dc} of the DAB. (b) Measured and the calculated transfer function between the control signal d_2 and the voltage v_{series} of the unfolder bridge.

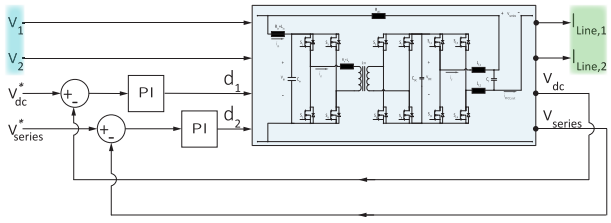

Fig. 5. PFCC with the closed-loop control of the dc link voltage V_{dc} and floating voltage V_{series}. The inputs to the PFCC large-signal model from the dc grid model are highlighted in the blue rectangle. The outputs of the PFCC large-signal model that are returned to the dc grid model are highlighted in the green rectangle.

Using (37) and (38), we can efficiently couple the PFCC large-signal model with the LVdc grid model.

B. Meshed Grid

In this section, the derived PFCC large-signal model is used together with the dc grid model to simulate a simple case, which can be, to a large extent, reproduced in the laboratory. The schematic of the grid used in the simulation is shown in Fig. 7. The case study is based on the ring/meshed grid topology and allows the power to circulate in the grid. The grid consists of four nodes, where nodes 1 and 2 are the output and the input of the PFCC, respectively. Nodes 3 and 4 are supplying or sinking the power in the grid. The power flows in the lines $P_{\text{Line},2}$ and $P_{\text{Line},3}$ are coupled as the nodes are not ideal voltage sources. The PFCC is used to inject the voltage in series with the line to change the amount of power flowing through different lines, as well as to change the direction of power in lines.

In the simulation, node 3 is modeled as a voltage source converter with dc grid side capacitance C_{Node}. Node 3 holds the voltage V_3 constant at 350 V. Node 4 is modeled as a constant power load, which is set to sink 4.5 kW and has the capacitance C_{Node} on the dc grid side. The rest of the parameters are shown in Table I.

In Fig. 6(a), the voltages in the simulated grid are shown. The voltage V_3 remains stable during the simulation.

TABLE I
PARAMETERS OF THE GRID USED FOR SIMULATION

Parameter	Acronym	Value
Line resistance 1	$R_{\text{Line},1}$	100 mΩ
Line resistance 2	$R_{\text{Line},2}$	1 Ω
Line resistance 3	$R_{\text{Line},3}$	2 Ω
Line inductance 1,2,3	L_{Line}	1 µH
Line capacitance 1,2,3	C_{Line}	10 nF
Node capacitance	C_{Node}	1 mF
Inner pfcc resistance	R_{pfc}	1 Ω
Nominal Node 3 Voltage	V_3	350 V
Nominal Node 4 Voltage	V_4	350 V

The voltage V_4 is changing as the node is programed to behave as a constant power load. The voltages V_1 and V_2 are the voltages at the input and output of the PFCC, respectively. In Fig. 6(b), the currents flowing in the grid are shown. Fig. 6(c) shows the powers flowing in the grid. The current direction defines the direction of the power flow. Arrows in Fig. 7 represent the direction convention.

The simulation starts with 0 V being injected in series with the line, during time interval Δt_1. The current flowing in line 3, $I_{\text{Line},3}$, is higher than the current flowing in the line containing the PFCC. During second time interval Δt_2, −10 V is injected in series with line 2. The series voltage increases the current flowing in line 3. The power flow in line 3 is reversed during fourth time interval Δt_4, when the PFCC injects 25 V. At this point, almost all the power between the nodes is flowing through line 2, $P_{\text{Line},2}$. The power flowing through line 3 is close to zero. Coincidently, in this case, the reduction of the power flow in line 3 makes the system more efficient as can be seen by the reduced power $P_{\text{Node},3}$.

C. Sensitivity of the Model to the Line Parameters

In Section II, a modeling approach was described, which allows to model the line inductance, line capacitance, line resistance, and even line conductance. It is interesting to

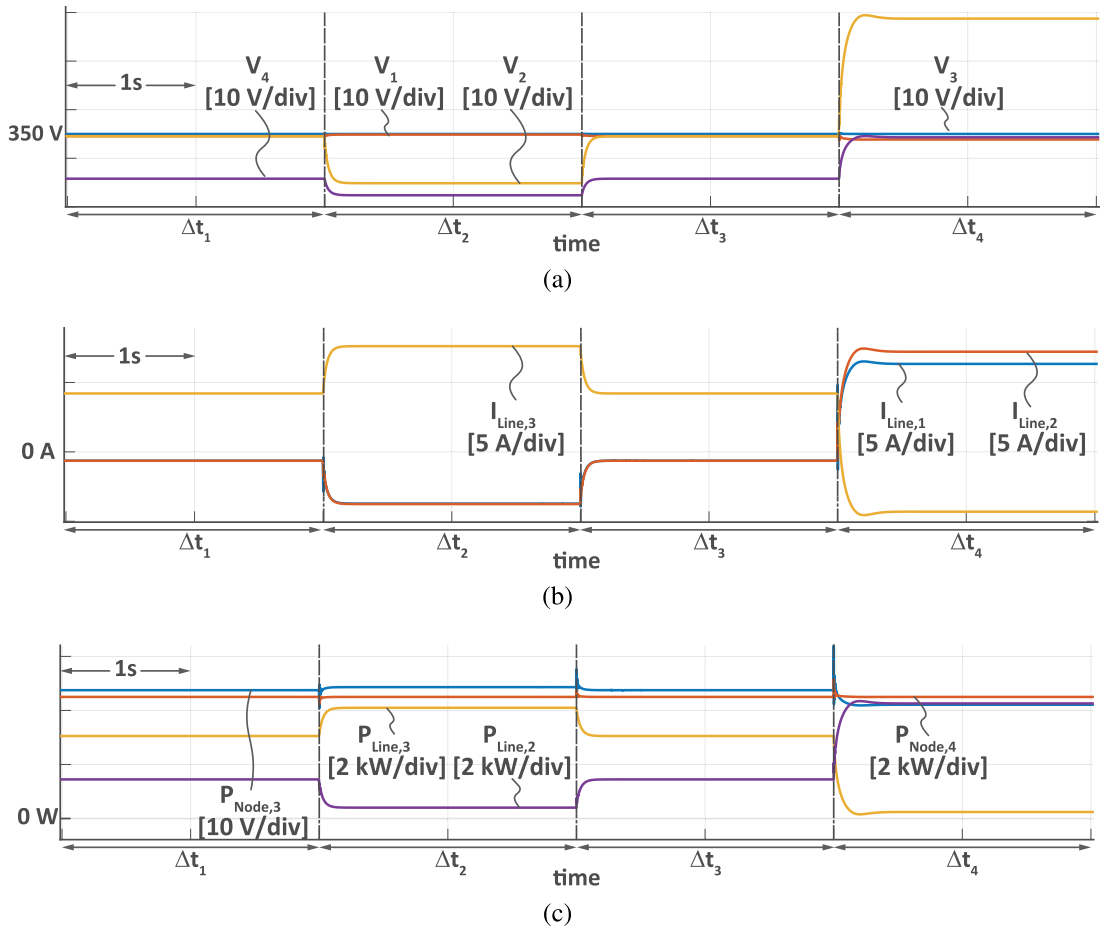

Fig. 6. At the start of the simulation, the injected voltage is zero, and the line resistances give the ratio between the currents in the lines. During the simulation, the power flow in the lines is altered by the PFCC. (a) Grid voltages. (b) Currents. (c) Powers.

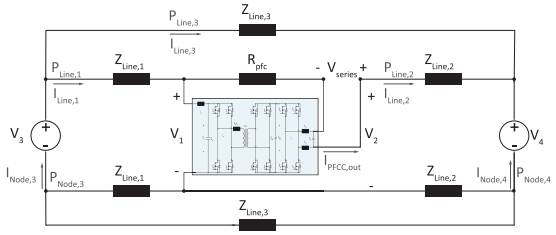

Fig. 7. Basic meshed grid, for simulation and experiment. In the simulation, node 3 is holding voltage V_3 constant, while node 4 works as a constant power load, i.e., voltage V_4 is not held constant. In the experiment, nodes 3 and 4 are emulated with laboratory power supplies SM15K.

investigate the influence of the line parameters on the operation of the PFCC due to several reasons. First, the PFCC must be designed to operate reliably under a range of line parameters, not just a single value. Second, the line parameters and impedances as discussed in the introduction influence the power rating of the PFCC. Last, the grid parameters influence the experiments. Therefore, before the simulation results are compared with the experimental data, it is vital to consider which parameters influence the results of the experiment significantly. The line conductance has virtually no influence in the small monopolar system on the system itself or the PFCC operation. Therefore, it can be disregarded. However, the other line parameters might influence the operation of both the grid and the PFCC.

Line resistance is a series parasitic element. The influence of this parameter is straightforward to asses. The higher the line resistance, the higher the voltage drop across it and less current can be pushed through for the same power level. In the experiments, this parameter can be controlled with precision up to hundredths of milliohm.

The influence of the line capacitance and line inductance is more difficult to assess. The influence of the line capacitance on the operation of the PFCC can be overshadowed by the size of the nodes' capacitances and the capacitances of the PFCC. During the experiments, the node and PFCC capacitances were much higher than the line capacitances, $C_{\text{node}} \gg C_{\text{line}}$. The small line capacitance is the result of small-cable cross sections and very short cable connections. Therefore, it can be concluded that the line capacitances have a negligible influence on the overall dynamics of the experiment.

The influence of the line inductances on the dynamics of the PFCC is analyzed via simulation of the system from the previous section. Fig. 8 shows the influence of the changing line inductance on the output current of the PFCC $I_{\text{Line},2}$. The increase in the line inductances slows down the change of

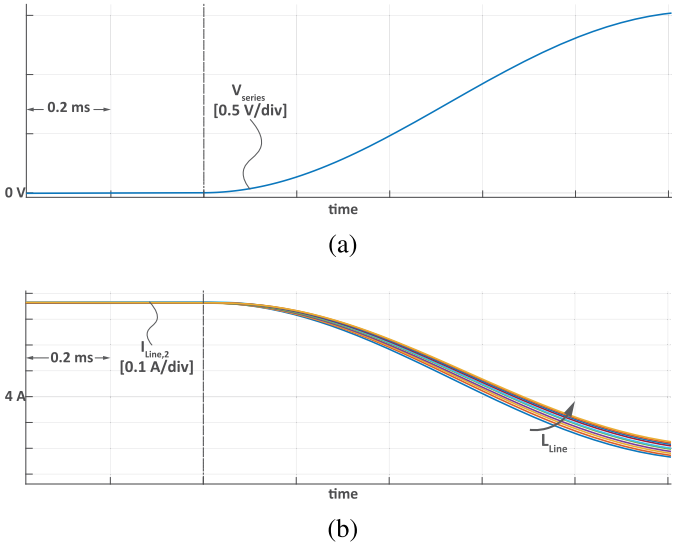

Fig. 8. Line inductance in each line was varied from 1 to 100 μH, and the different system response to a disturbance was observed. The disturbance is the change of the injected series voltage. (a) Series voltage. (c) Current flowing out of the PFCC in line 2.

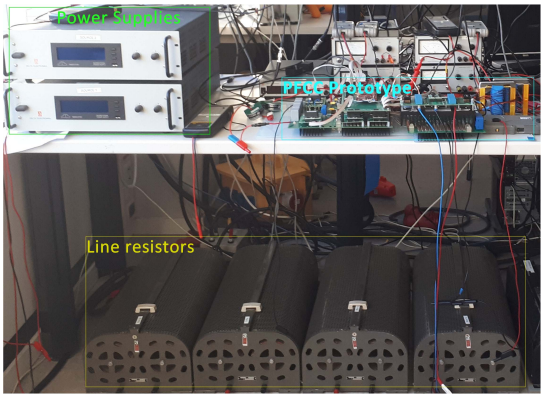

Fig. 9. Experimental setup.

the output current. In Fig. 8(b), the variation of the output current of the PFCC is evident. It is critical to address as, during the experimental measurements, the line inductances are frequency-dependent parasitic elements and as such challenging to measure precisely, and their influence can be in the range of tens of milliamperes.

IV. Experiment

The closed-loop control of the PFCC is implemented in a *C2000 Delfino LaunchPad*. The MOSFETs used for the HV side of the DAB are C3M0075120J. The MOSFETs used on the low-voltage side of the PFCC are IPB027N10N3GATMA1. The parameters of the prototype are summarized in Table II, and the grid parameters are the same as in Table I. The experimental setup is shown in Fig. 9.

During all experiments in this paper, Delta Elektronika SM15K power supplies are used to emulate the nodes (sources). Since, in a real meshed LVdc grid, there are typically more lines than voltage controlling converters,

TABLE II
Design Parameters of the PFCC Prototype

Parameter	Acronym	Value
Nominal Input Voltage	$V_{in,nom}$	350 [V]
Nominal DC-link Voltage	V_{dc}	50 [V]
Transformer ratio	n	7 [-]
Switching Frequency	f_s	83 [kHz]
Parasitic Inductance	L_σ	78 [μH]
Input DC Capacitor	C_{in}	16 [μF]
DC-link Capacitor	C_{DC}	1.22 [mF]
Unfolder Bridge Inductor	$L_{f,i}$	31 [μH]
Unfolder Bridge Capacitor	C_f	1.22 [mF]

the resulting power flows are coupled. To mimic the meshed LVdc grid, the power flows in lines $P_{\text{Line},2}$ and $P_{\text{Line},3}$ are coupled.

A. Comparison of Simulation and Experimental Results

The small-signal model derived in Section II was validated via measurement of the transfer functions. The dc grid model with the large-signal PFCC model is validated in this section in the time domain. The laboratory-scale microgrid is schematically shown in Fig. 7. The voltages V_3 and V_4 are programed for the same initial voltage of 350 V. The voltage reference V^*_{series} is stepped from 0 to 5 V at the time instance t_{step}. The experiment is repeated with different V_{series} PI controller parameters.

Fig. 10 shows a comparison between the prototype and the simulation reacting to the step change in the V^*_{series} value from 0 to 5 V at time instance t_{step}. The experiment and simulation were repeated with different PI controller values for the unfolder bridge control loop. The faster controller is shown in Fig. 10(a). The controller with the coefficients reduced by one-fourth is shown in Fig. 10(b). Overall, the match between the simulation and the measurement in Fig. 10 is excellent. Fig. 10(a) and (b) show only small variations in the peak values during transients. The models obtained with the generalized averaging method are known to be precise up to one-third of the switching frequency [21]. The slight difference between the measured current and simulated current can be attributed to the fact that the line inductance influences the current dynamics as was studied in the previous section. Second, the differences partially arise from the measurement method itself. The current was measured with a clamp-on probe, for which the repeatability error up to 100 mA is common [43].

The small differences in voltage comparison can, besides the error stemming from repeatability of the measurement, be attributed to the fact that the equivalent series resistance of the capacitor is not modeled [21] and slight variations of the output capacitance. The output capacitor is made of parallel-connected ceramic capacitors, whose capacitance is dependent on voltage, frequency, and temperature. Last, the Delta Elektronika output capacitance and their internal control parameters are virtually unknown, and it is reasonable

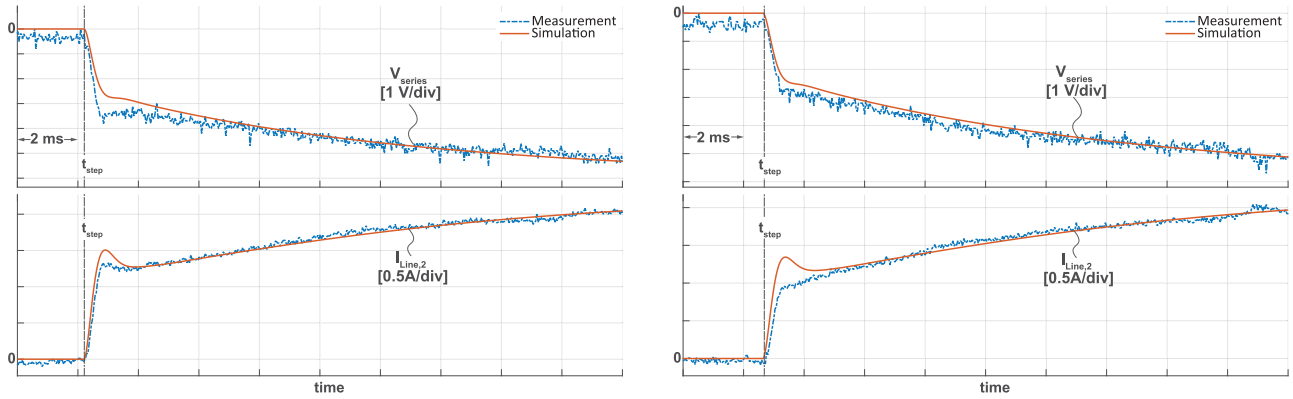

Fig. 10. Comparison of the series voltage step change—model and measured data. (a) Results when the PI parameters of the unfolder bridge $K_{\text{unf},1} = 1$ p.u. and $K_{\text{unf},2} = 1$ p.u.. (b) Results the PI parameters of the unfolder bridge $K_{\text{unf},1} = 0.8$ p.u. and $K_{\text{unf},2} = 0.8$ p.u.. In both the cases, the series voltage and current flowing in out of the PFCC (in line 2) are compared.

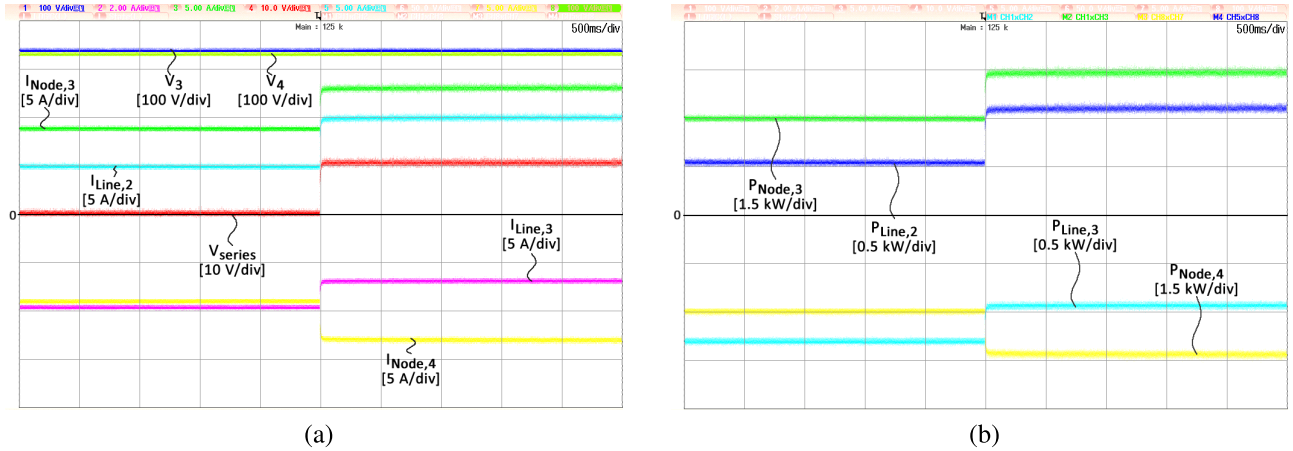

Fig. 11. Operation of the PFCC in a meshed microgrid demonstrating step-up of the power flow in the grid. (a) Voltages and currents of the microgrid. (b) Powers.

to assume that there is a small discrepancy due to these differences.

In summary, the match between the measurements and simulation in Fig. 4(a) and (b) gives confidence in the models presented in Section II. The comparison exhibits only small discrepancies of the peak values during transients, which can have several origins due to the complexity of the measured system.

B. Test in Meshed Grid

The experiment in this section will demonstrate the functionality of the PFCC in the laboratory-scale microgrid. The schematic from Fig. 7 is recreated in the laboratory. During the experiment, one power supply is programed with initial voltage V_3 of 350 V while the second power supply is programed with an initial voltage V_4 of 335 V. Contrary to the simulation, the Delta Elektronika power supplies do not behave as ideal constant power loads or sources. Therefore, some change in the operation can be observed. Nevertheless, they do allow to study the dynamics of the modeled PFCC and demonstrate its functionality.

As shown in Figs. 11–13, the voltages and the currents flow in the laboratory microgrid and inside the PFCC during the experiment. The experiment is separated in two main steps. First, the power flow in the grid is increased by the PFCC. In Fig. 11(a), the currents and voltages are shown, while, in Fig. 11(b), the powers during the increase of the power flow are shown. The power supplied by one source during this experiment is 4.5 kW. From Fig. 11(a), it is observable that the injected voltage V_{series} is 10 V, while the current flowing out of the PFCC $I_{\text{Line},2}$ is 10 A. This implies that the power processed by the PFCC is around 100 W. Fig. 11(b) explicitly shows that after injection of the series voltage, the power supplied by source one is increased by 1500 W. Clearly, the PFCC is capable of controlling significant power flow while processing only a fraction of the total system power.

The power supplied to the grid is 45 times higher than the power processed by the PFCC prototype. The difference in the power flow in line 2 after the PFCC injects 10 V is 15 times higher than the power processed by the PFCC prototype. These ratios show that partially rated PFCC can control grid power flow in a wide range. It also hints that the PFCC needs to

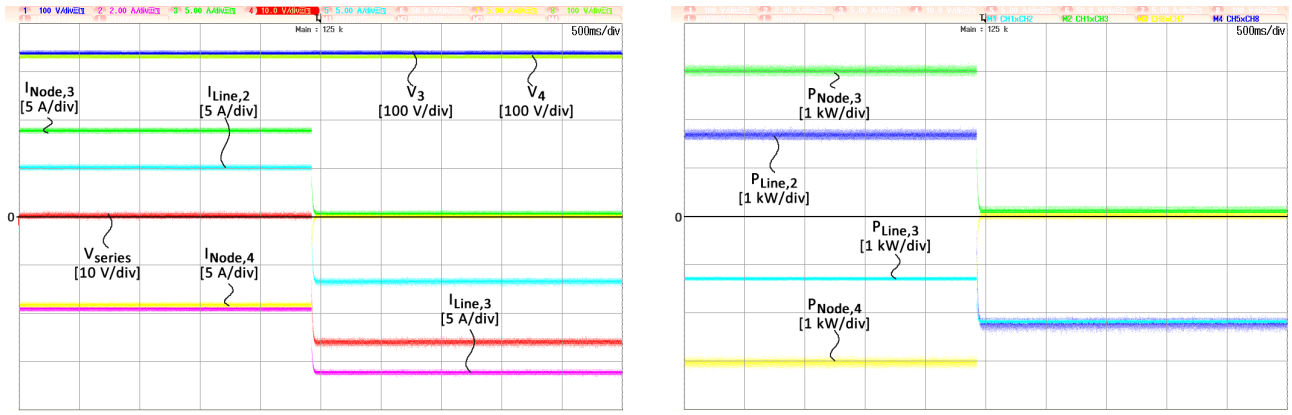

Fig. 12. Operation of the PFCC in a meshed microgrid demonstrating step-down of the power flow in the grid. (a) Voltages and currents of the microgrid. (b) Powers.

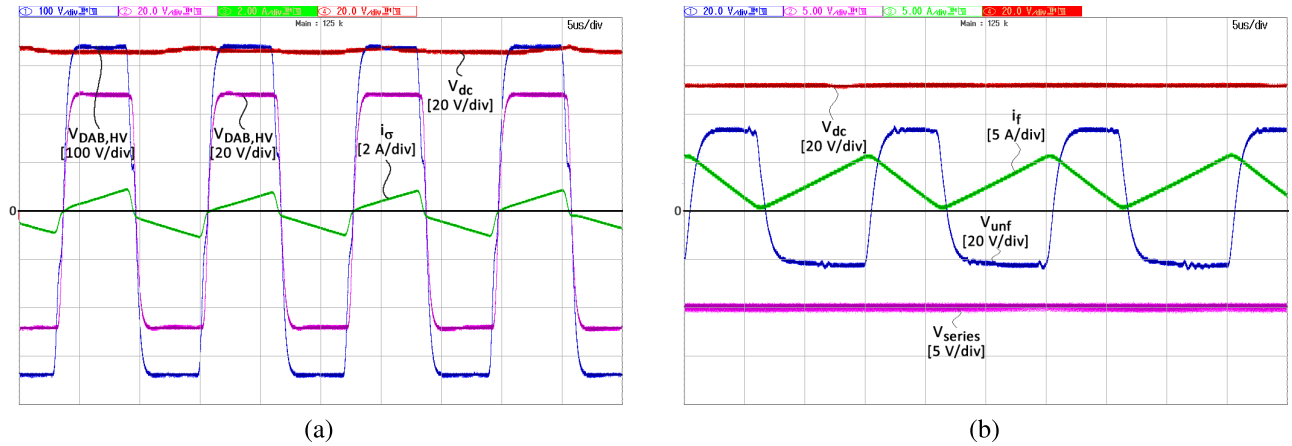

Fig. 13. Operational waveforms of (a) DAB and (b) unfolder bridge.

be able to operate with high power efficiency even when it is processing minimum powers. Therefore, it is advantageous to employ a DAB which can achieve a flat efficiency curve across a wide power range.

In the second experiment, the PFCC reduces the circulating power. The currents and voltages are shown in Fig. 12(a) and the powers are shown in Fig. 12(b). It is notable that the current flowing in line 2 $I_{\text{Line},2}$ is reversed during this experiment.

The measurement section is completed with the operating waveforms of the DAB, and the unfolder bridge, which are provided in Fig. 13(a) and (b), respectively.

V. Conclusion

The paper presents the derivation of the large- and small-signal models of the partially rated PFCC coupled with the LVdc distribution grid model. The PFCC model can be easily combined with the LVdc grid model and allows for fast algorithmization and easy simulation of the LVdc systems based on the decentralized power generation with the power flow controlled by the PFCC. Using the derived PFCC small-signal model, a simple controller was designed, in which specifics of the chosen topology were considered. The PFCC large-signal model was coupled with the LVdc network model to study the power flow control with a partially rated converter. The small-signal model was validated by measuring the control-to-output transfer functions. The PFCC large-signal model with dc grid model was validated with time domain measurements. The experiments also demonstrated the functionality of the PFCC in a LVdc grid. The proposed continuous full-order models are insightful and allow for controller design which takes into account the characteristics of the LVdc network, as well as the peculiarities of the PFCC operation.

Due to the nature of the multiterminal LVdc grids, the power flows are coupled. Therefore, tools to study modeling and control of the power flows are necessary to further the applicability of the LVdc for the electric energy distribution. The effects of the PFCC on the LVdc grid dynamics and the effects of the LVdc grid dynamics on the PFCC can be easily studied with the presented models. Furthermore, the models can be used for the design of novel power flow control algorithms based on a partially rated PFCC, which can further increase the appeal of multiterminal LVdc grids. The models can serve as a basis for studying truly decentralized grid topologies that allow for the

integration of microgrids with significant numbers of cheap and efficient power flow control units.

REFERENCES

[1] G. R. C. Mouli, P. Venugopal, and P. Bauer, "Future of electric vehicle charging," in *Proc. Int. Symp. Power Electron. (Ee)*, Oct. 2017, pp. 1–7.

[2] T. Dragicevic, J. C. Vasquez, J. M. Guerrero, and D. Skrlec, "Advanced LVDC electrical power architectures and microgrids: A step toward a new generation of power distribution networks," *IEEE Electrific. Mag.*, vol. 2, no. 1, pp. 54–65, Mar. 2014.

[3] D. Boroyevich, R. Burgos, L. Arnedo, and F. Wang, "Synthesis and integration of future electronic power distribution systems," in *Proc. Power Convers. Conf.-Nagoya*, Apr. 2007, pp. K-1–K-8.

[4] J. M. Guerrero, J. C. Vasquez, J. Matas, L. G. de Vicuna, and M. Castilla, "Hierarchical control of droop-controlled AC and DC microgrids—A general approach toward standardization," *IEEE Trans. Ind. Electron.*, vol. 58, no. 1, pp. 158–172, Jan. 2011.

[5] A. Werth, N. Kitamura, and K. Tanaka, "Conceptual study for open energy systems: Distributed energy network using interconnected DC nanogrids," *IEEE Trans. Smart Grid*, vol. 6, no. 4, pp. 1621–1630, Jul. 2015.

[6] B. Wunder, L. Ott, M. Szpek, U. Boeke, and R. Weiß, "Energy efficient DC-grids for commercial buildings," in *Proc. IEEE 36th Int. Telecommun. Energy Conf. (INTELEC)*, Sep./Oct. 2014, pp. 1–8.

[7] L. Mackay, N. H. van der Blij, L. Ramirez-Elizondo, and P. Bauer, "Toward the universal DC distribution system," *Electr. Power Compon. Syst.*, vol. 45, no. 10, pp. 1032–1042, 2017.

[8] N. Hatziargyriou, H. Asano, R. Iravani, and C. Marnay, "Microgrids," *IEEE Power Energy Mag.*, vol. 5, no. 4, pp. 78–94, Jul./Aug. 2007.

[9] X. Lu, J. M. Guerrero, K. Sun, and J. C. Vasquez, "An improved droop control method for DC microgrids based on low bandwidth communication with DC bus voltage restoration and enhanced current sharing accuracy," *IEEE Trans. Power Electron.*, vol. 29, no. 4, pp. 1800–1812, Apr. 2014.

[10] N. Bottrell, M. Prodanovic, and T. C. Green, "Dynamic stability of a microgrid with an active load," *IEEE Trans. Power Electron.*, vol. 28, no. 11, pp. 5107–5119, Nov. 2013.

[11] A. P. N. Tahim, D. J. Pagano, E. Lenz, and V. Stramosk, "Modeling and stability analysis of islanded DC microgrids under droop control," *IEEE Trans. Power Electron.*, vol. 30, no. 8, pp. 4597–4607, Aug. 2015.

[12] N. H. van der Blij, L. M. Ramirez-Elizondo, M. T. J. Spaan, and P. Bauer, "A state-space approach to modelling DC distribution systems," *IEEE Trans. Power Syst.*, vol. 33, no. 1, pp. 943–950, Jan. 2018.

[13] C. Kumar and M. Liserre, "A new prospective of smart transformer application: Dual microgrid (DMG) operation," in *Proc. 41st Annu. Conf. IEEE Ind. Electron. Soc. (IECON)*, Nov. 2015, pp. 4482–4487.

[14] M. Stieneker and R. W. De Doncker, "Medium-voltage DC distribution grids in urban areas," in *Proc. IEEE 7th Int. Symp. Power Electron. Distrib. Gener. Syst. (PEDG)*, Jun. 2016, pp. 1–7.

[15] Q. Shafiee, T. Dragicevic, J. C. Vasquez, and J. M. Guerrero, "Modeling, stability analysis and active stabilization of multiple DC-microgrid clusters," in *Proc. IEEE Int. Energy Conf. (ENERGYCON)*, May 2014, pp. 1284–1290.

[16] S. Anand and B. G. Fernandes, "Reduced-order model and stability analysis of low-voltage DC microgrid," *IEEE Trans. Ind. Electron.*, vol. 60, no. 11, pp. 5040–5049, Nov. 2013.

[17] T. Pavlovic, T. Bjazic, and Z. Ban, "Simplified averaged models of DC–DC power converters suitable for controller design and microgrid simulation," *IEEE Trans. Power Electron.*, vol. 28, no. 7, pp. 3266–3275, Jul. 2013.

[18] H. K. Krishnamurthy and R. Ayyanar, "Building block converter module for universal (AC-DC, DC-AC, DC-DC) fully modular power conversion architecture," in *Proc. IEEE Power Electron. Spec. Conf.*, Jun. 2007, pp. 483–489.

[19] F. Krismer and J. W. Kolar, "Accurate small-signal model for an automotive bidirectional dual active bridge converter," in *Proc. 11th Workshop Control Modeling Power Electron.*, Aug. 2008, pp. 1–10.

[20] C. Zhao, S. D. Round, and J. W. Kolar, "Full-order averaging modelling of zero-voltage-switching phase-shift bidirectional DC–DC converters," *IET Power Electron.*, vol. 3, no. 3, pp. 400–410, May 2010.

[21] H. Qin and J. W. Kimball, "Generalized average modeling of dual active bridge DC–DC converter," *IEEE Trans. Power Electron.*, vol. 27, no. 4, pp. 2078–2084, Apr. 2012.

[22] J. A. Mueller and J. W. Kimball, "An improved generalized average model of DC–DC dual active bridge converters," *IEEE Trans. Power Electron.*, vol. 33, no. 11, pp. 9975–9988, Nov. 2018.

[23] J. A. Mueller and J. W. Kimball, "Modeling dual active bridge converters in DC distribution systems," *IEEE Trans. Power Electron.*, vol. 34, no. 6, pp. 5867–5879, Jun. 2018.

[24] L. Mackay, T. Hailu, L. Ramirez-Elizondo, and P. Bauer, "Decentralized current limiting in meshed DC distribution grids," in *Proc. IEEE 1st Int. Conf. Direct Current Microgrids (ICDCM)*, Jun. 2015, pp. 234–238.

[25] M. Hajian, D. Jovcic, G. Asplund, and H. Zhang, "Power flow control in DC transmission grids using mechanical and semiconductor based DC/DC devices," in *Proc. 10th IET Int. Conf. AC and DC Power Transmiss. (ACDC)*, 2012, p. 43.

[26] Q. Mu, J. Liang, Y. Li, and X. Zhou, "Power flow control devices in DC grids," in *Proc. IEEE Power Energy Soc. Gen. Meeting*, Jul. 2012, pp. 1–7.

[27] K. Rouzbehi, J. I. Candela, A. Luna, G. Gharehpetian, and P. Rodriguez, "Flexible control of power flow in multiterminal DC grids using DC–DC converter," *IEEE J. Emerg. Sel. Topics Power Electron.*, vol. 4, no. 3, pp. 1135–1144, Sep. 2016.

[28] D. Jovcic and B. T. Ooi, "Developing DC transmission networks using DC transformers," *IEEE Trans. Power Del.*, vol. 25, no. 4, pp. 2535–2543, Oct. 2010.

[29] L. Yao, H. Cui, J. Zhuang, G. Li, B. Yang, and Z. Wang, "A DC power flow controller and its control strategy in the DC grid," in *Proc. IEEE 8th Int. Power Electron. Motion Control Conf. (IPEMC-ECCE Asia)*, May 2016, pp. 2609–2614.

[30] P. Purgat, L. Mackay, R. A. Prakoso, L. Ramirez-Elizondo, and P. Bauer, "Power flow control converter for meshed LVDC distribution grids," in *Proc. IEEE 2nd Int. Conf. DC Microgrids (ICDCM)*, Jun. 2017, pp. 476–483.

[31] P. Purgat, R. A. Prakoso, L. Mackay, Z. Qin, L. Ramirez-Elizondo, and P. Bauer, "A partially rated DC–DC converter for power flow control in meshed LVDC distribution grids," in *Proc. IEEE Appl. Power Electron. Conf. Exposit. (APEC)*, Mar. 2018, pp. 1591–1596.

[32] L. Gyugyi, C. D. Schauder, S. L. Williams, T. R. Rietman, D. R. Torgerson, and A. Edris, "The unified power flow controller: A new approach to power transmission control," *IEEE Trans. Power Del.*, vol. 10, no. 2, pp. 1085–1097, Apr. 1995.

[33] J. A. Cobos, H. Cristóbal, D. Serrano, R. Ramos, J. A. Oliver, and P. Alou, "Differential power as a metric to optimize power converters and architectures," in *Proc. IEEE Energy Convers. Congr. Expo. (ECCE)*, Oct. 2017, pp. 2168–2175.

[34] P. Purgat, L. Mackay, Z. Qin, and P. Bauer, "On the protection of the power flow control converter in meshed low voltage DC networks," in *Proc. IEEE Energy Convers. Congr. Expo. (ECCE)*, Sep. 2018, pp. 478–484.

[35] K. Rouzbehi, A. Miranian, J. I. Candela, A. Luna, and P. Rodriguez, "A hybrid power flow controller for flexible operation of multi-terminal DC grids," in *Proc. Int. Conf. Renew. Energy Res. Appl. (ICRERA)*, Oct. 2014, pp. 550–555.

[36] K. Rouzbehi, A. Miranian, J. I. Candela, A. Luna, and P. Rodriguez, "Proposals for flexible operation of multi-terminal DC grids: Introducing flexible DC transmission system (FDCTS)," in *Proc. Int. Conf. Renew. Energy Res. Appl. (ICRERA)*, Oct. 2014, pp. 180–184.

[37] N. H. van der Blij, L. M. Ramirez-Elizondo, M. T. J. Spaan, and P. Bauer, "A state-space approach to modelling DC distribution systems," *IEEE Trans. Power Syst.*, vol. 33, no. 1, pp. 943–950, Jan. 2018.

[38] C. R. Paul, *Analysis of Multiconductor Transmission Lines*, 2nd ed. Hoboken, NJ, USA: Wiley, 2007.

[39] S. R. Sanders, J. M. Noworolski, X. Z. Liu, and G. C. Verghese, "Generalized averaging method for power conversion circuits," *IEEE Trans. Power Electron.*, vol. 6, no. 2, pp. 251–259, Apr. 1991.

[40] H. Qin and J. W. Kimball, "Closed-loop control of DC–DC dual-active-bridge converters driving single-phase inverters," *IEEE Trans. Power Electron.*, vol. 29, no. 2, pp. 1006–1017, Feb. 2014.

[41] S. Synkule, L. Heinzle, F. Hecht, and F. Hämmerle, "DC/DC converter stability measurement," OMICRON Lab, USA, Tech. Rep., Dec. 2017. [Online]. Available: http://literature.cdn.keysight.com/litweb/pdf/5991-4375EN.pdf

[42] R. P. Aguilera, P. Acuna, G. Konstantinou, S. Vazquez, and J. I. Leon, "Chapter 2—Basic control principles in power electronics: Analog and digital control design," in *Control of Power Electronic Converters and Systems*, F. Blaabjerg, Ed. New York, NY, USA: Academic, 2018, pp. 31–68.

[43] "Evaluating current probe technologies for low-power measurements," Keysight Technol., Santa Rosa, CA, USA Dec. 2017.

Pavel Purgat (S'16) received the B.Sc. degree in electrical engineering from Czech Technical University, Prague, Czech Republic, in 2014, the M.Sc. degree in electrical engineering from the Delft University of Technology, Delft, Netherlands, with focus on power electronics and inductive power transfer control, in 2016, where he is currently pursuing the Ph.D. degree.

In 2017, he was a Visiting Researcher with Fraunhofer-IISB, Erlangen, Germany. His current research interests include power electronics and power electronics intensive applications.

Nils H. van der Blij (S'16) was born in Leiden, The Netherlands, in 1990. He received the bachelor's and master's degrees in electrical engineering from the Delft University of Technology, Delft, The Netherlands, in 2011 and 2013, respectively, where he is currently pursuing the Ph.D. degree in management and control of dc distribution grids.

His research experience includes Scarabee, Hoofddorp, The Netherlands, Philips, Eindhoven, The Netherlands, Cambridge University, Cambridge, U.K., and Delft University of Technology, Delft, The Netherlands. His current research interests include dc distribution grids, electrical machines and drives, and sustainable energy generation.

Zian Qin (S'13–M'15) received the B.Eng. degree in automation from Beihang University, Beijing, China, in 2009, the M.Eng. degree in control science and engineering from the Beijing Institute of Technology, Beijing, in 2012, and the Ph.D. degree from Aalborg University, Aalborg, Denmark, in 2015.

In 2014, he was a Visiting Scientist with Aachen University, Aachen, Germany. From 2015 to 2017, he was a Post-Doctoral Research Fellow with Aalborg University. He is currently an Assistant Professor with the Delft University of Technology, Delft, The Netherlands. His current research interests include power electronics and power electronics grid.

Pavol Bauer (SM'07) is currently a Full Professor with the Department of Electrical Sustainable Energy, Delft University of Technology, where he is also the Head of the DC Systems, Energy Conversion and Storage Group. He has authored or coauthored more than 72 journal and almost 300 conference papers in his field (with H factor Google scholar 30, Web of science 18) and 8 books. He holds four international patents and organized several tutorials at the international conferences. He has worked on many projects for industry concerning wind and wave energy, power electronic applications for power systems such as Smarttrafo; HVdc and LVdc systems, projects for smart cities such as PV charging of electric vehicles, PV and storage integration, contactless charging; and he participated in several Leonardo da Vinci and H2020 EU projects as project partner (ELINA, INETELE, and E-Pragmatic) and coordinator (PEMCWebLab.com-Edipe, SustEner, and Eranet DCMicro).

Mr. Bauer is a member of the Executive Committee of European Power Electronics Association (EPE) and international steering committee at numerous conferences. He is a former Chairman of Benelux IEEE Joint Industry Applications Society and Power Electronics and Power Engineering Society Chapter, the Chairman of the Power Electronics and Motion Control (PEMC) council.